Volume 1 | Number 1 | Jan 2013 | Pages 1–100

Nanoscale

www.rsc.org/nanoscale

ROYAL SOCIETY OF CHEMISTRY

This is an *Accepted Manuscript*, which has been through the Royal Society of Chemistry peer review process and has been accepted for publication.

Accepted Manuscripts are published online shortly after acceptance, before technical editing, formatting and proof reading. Using this free service, authors can make their results available to the community, in citable form, before we publish the edited article. We will replace this *Accepted Manuscript* with the edited and formatted *Advance Article* as soon as it is available.

You can find more information about *Accepted Manuscripts* in the **Information for Authors**.

Please note that technical editing may introduce minor changes to the text and/or graphics, which may alter content. The journal's standard **Terms & Conditions** and the **Ethical guidelines** still apply. In no event shall the Royal Society of Chemistry be held responsible for any errors or omissions in this *Accepted Manuscript* or any consequences arising from the use of any information it contains.

www.rsc.org/nanoscale

Graphdiyne-metal contacts and graphdiyne transistors

Yuanyuan Pan[1,†], Yangyang Wang[1,†], Lu Wang[4], Hongxia Zhong[1], Ruge Quhe[1,3], Zeyuan Ni[1],

Meng Ye[1], Wai-Ning Mei[4], Junjie Shi[1], Wanlin Guo[5], Jinbo Yang[1,2] *, Jing Lu[1,2] *

[1]State Key Laboratory of Mesoscopic Physics and Department of Physics,

Peking University, Beijing 100871, P. R. China

[2]Collaborative Innovation Center of Quantum Matter, Beijing 100871, P. R. China

[3]Academy for Advanced Interdisciplinary Studies, Peking University, Beijing 100871,

P. R. China

[4]Department of Physics, University of Nebraska at Omaha, Omaha, Nebraska 68182-0266

[5]State Key Laboratory of Mechanics and Control of Mechanical Structures, Key Laboratory for

Intelligent Nano Materials and Devices of the Ministry of Education, and Institute of Nanoscience,

Nanjing University of Aeronautics and Astronautics, Nanjing 210016, P. R. China

[†]These authors contributed equally to this work.

* Corresponding authors: jinglu@pku.edu.cn, jbyang@pku.edu.cn

ABSTRACT

Graphdiyne is prepared on metal surface, and making devices out of it inevitably involves contact with metals. Using density functional theory with dispersion correction, we systematically studied for the first time the interfacial properties of graphdiyne contacting with a series of metals (Al, Ag, Cu, Au, Ir, Pt, Ni, and Pd). Graphdiyne is in an n-type Ohmic or quasi-Ohmic contact with Al, Ag, and Cu, while it is in a Schottky contact with Pd, Au, Pt, Ni, and Ir (at source/drain-channel interface), with high Schottky barrier heights of 0.21, 0.46, (n-type), 0.30, 0.41, and 0.46 (p-type) eV, respectively. A graphdiyne field effect transistor (FET) with Al electrodes is simulated by using quantum transport calculations. This device exhibits an on-off ratio up to 10^4 and a very large on-state current of 1.3×10^4 mA/mm in a 10 nm channel length. Thus, a new prospect is opened up for graphdiyne in high performance nanoscale devices.

Due to three hybridization states (sp^1, sp^2 and sp^3), carbon can form a set of allotropes, such as fullerenes,[1] carbon nanotubes,[2] and graphene.[3] Graphene has significant potential application in the nanoelectronics because of its high carrier mobility. However, the zero band gap limits its application in effective field effect transistor (FET). In spite of the fact that additional efforts such as applying an electric field or single-side adsorption of atoms/molecules on bilayer and ABC-stacked few-layer graphene[4] or sandwiching graphene by BN single layer have been done,[5] opening a large band gap without degrading its electronic properties remains a tough challenge for graphene. As a novel two-dimensional carbon allotrope that has both sp^1 and sp^2 carbon atoms,[6,7] graphdiyne was first prepared by Li's group on the Cu surface via a cross-coupling reaction using hexaethynylbenzene in 2009.[8] It has a conductivity of 2.516×10^{-4} S/m, typical of a semiconductor. The calculated band gap at the density functional theory (DFT) level is about 0.5 eV.[9] The calculated in-plane intrinsic electron and hole mobility in graphdiyne can reach the order of 10^5 and 10^4 $cm^2V^{-1}s^{-1}$,[10] respectively, at room temperature, which are comparable with those of graphene. As one atomic layer thick material, short-channel effects are expected to be greatly suppressed in graphdiyne,[11] and a FET based on graphdiyne probably can be scaled down to very short channel length. Therefore, graphdiyne is a promising candidate material for high-speed applications in logic devices. To date, most previous studies about graphdiyne have focused mainly on the electronic, optical, and mechanical properties,[9,12,13,14,15] or the application in hydrogen purification and storage,[16] solar cells,[17] photocatalytics,[18] anode of lithium batteries,[19,20] and efficient field emission[21] etc. Very little attention was paid to its FET performance.

As we all know, fabricating devices out of graphdiyne inevitably involves contact with metal electrodes, and good contact always improves device performance remarkably. Together with the fact that graphdiyne is prepared on the Cu substrate, it is of fundamental interest to explore the graphdiyne-metal contacts from theoretical aspect. However, to the best of our knowledge, the interfacial properties of graphdiyne on metals remain an open question.

In this paper, we systematically study for the first time the interfacial properties of graphdiyne on a variety of metals (Al, Ag, Cu, Au, Ir, Pt, Ni, and Pd) by using DFT. The band

structure of graphdiyne is destroyed on Ir, Pt, Ni, and Pd surfaces as a result of a chemisorption, but is preserved on Al, Ag, Cu, and Au surfaces as a result of a physisorption. Al, Ag, and Cu electrodes are in an Ohmic or quasi-Ohmic contact with graphdiyne, while Pd, Pt, Ni, Ir, and Au electrodes are in a Schottky contact with it. Subsequently, a graphdiyne FET device with Al electrodes is simulated by using the quantum transport approach. The 10 nm-channel-length graphdiyne FET reveals an on-off ratio up to 10^4, suggestive of the great potential of graphdiyne as the channel of a high performance nanoscale FET.

Computational details

We choose five layers of metal atoms (Al, Ag, Cu, Au, Ir, Pt, Ni, and Pd) in (111) orientation to simulate the metal surfaces which cover a wide range of workfunction and construct a supercell with graphdiyne absorbed on one side of the metal surfaces, as shown in Fig. 1. We fix the in-plane lattice constant of graphdiyne to the value $a = 9.45$ Å.[22] The $2\sqrt{3} \times 2\sqrt{3}$ unit cells of Al, Ag, Cu, Au, Pt, and Pd (111) and the 4×4 unit cells of Ir and Ni (111) faces are adjusted to graphdiyne 1×1 unit cell, respectively. The lattice constant mismatches are 0.96 ~ 6.31%, as given in Table 1. A vacuum buffer space of at least 15 Å is set. Graphdiyne mainly interacts with the topmost two layers metal atoms, so cell shape and the bottom three layers of metal atoms are fixed.

The geometry optimizations and energy of optimized configuration are performed with the ultrasoft pseudopotentials plane-wave basis set with cut-off energy of 240 and 310 eV separately, implemented in the CASTEP code.[23] Generalized gradient approximation[24] (GGA) of PBE form to the exchange-correlation functional is used. Take into account Van der Waals force, a DFT-D dispersion-correction approach is adopted.[25] The electronic structure calculations are analyzed via additional calculations based on the plane-wave basis set with a cut-off energy of 400 eV and the projector-augmented wave (PAW) pseudopotential[26] implemented in the Vienna *ab initio* simulation package (VASP) code.[27] [28] To obtain reliable optimized structures, the maximum residual force is less than 0.01 eV/Å and energies are converged to within 5×10^{-6} eV per atom. The Monkhorst-Pack k-point mesh[29] is sampled with a separation of about 0.02 Å^{-1} in the Brillouin zone during the relaxation and electronic calculation periods.

Transport properties are calculated by using SE extended Hückel method coupled with nonequilibrium Green's function (NEGF) method, which are implemented in Atomistix Tool Kit (ATK) 11.2 package.[30,31,32] Hoffman basis set is used, the real-space mesh cutoff is 270 eV, and the temperature is set at 300 K. The electronic structures of electrodes and central region are calculated with a Monkhorst–Pack[29] $50 \times 1 \times 50$ and $50 \times 1 \times 1$ k-point grid, respectively. The zero-bias conductance and the current at a finite bias are given by the Landauer-Büttiker formula:[33]

$$\sigma(V_g) = \frac{2e^2}{h} \int T_{V_g}(E, V_{bias} = 0) f'(E\text{-}E_f) dE \approx \frac{2e^2}{h} T_{V_g}(E_f, V_{bias} = 0) \tag{1}$$

$$I(V_g, V_{bias}) = \frac{2e}{h} \int_{-\infty}^{+\infty} \{T_{V_g}(E, V_{bias})[f_L(E - \mu_L) - f_R(E - \mu_R)]\} dE \tag{2}$$

where $T_{V_g}(E, V_{bias})$ is the transmission probability at a given gate voltage V_g and bias voltage V_{bias}, $f_{L/R}$ the Fermi-Dirac distribution function for the left (L)/right (R) electrode, and $\mu_{L/R}$ the electrochemical potential of the L/R electrode, and $\mu_{L/R} = E_F \pm V_{bias}/2$. GGA) of PBE form[24] to the exchange-correlation functional is used through this paper.

Results and Discussions

Graphdiyne-metal contacts

Three initial configurations are considered for graphdiyne on Au surface, with the center of the carbon hexagon of graphdiyne on the top of A (the first), B (the second), and C (the third) layers of Au surface, respectively, as shown in Fig. 1. After relaxation, the configuration with the center of the carbon hexagon of graphdiyne on the top of A layer metal atoms has the lowest energy, and the relaxation of graphdiyne on other metal surfaces also starts from this configuration. The other two configurations are 0.15 and 0.14 eV/supercell higher in energy, respectively. The optimized structures of graphdiyne adsorbed on all metal surfaces after relaxation are shown in Fig. 2. There are distinct buckling heights of graphdiyne on the interfaces. The buckling heights of graphdiyne adsorbed on Au, Ag, Al, Cu, and Ir surfaces are smaller with values of 0.01, 0.02, 0.05, 0.09, and 0.13 Å, respectively, while on Ni, Pd, and Pt surfaces are larger with values of 0.58, 0.70, and 0.88 Å, respectively. As for the metal surfaces, the buckling of the A layer of Ir, Cu, Al, and Ag is small with buckling heights less

than 0.13 Å in the vertical direction, while there is apparent buckling of the A layer for Pt, Ni, Pd, and Au with buckling heights of 0.36, 0.37, 0.43, and 0.73 Å in the vertical direction of the interface, separately.

The key parameters of graphdiyne-metal contacts are listed in Table 1. The binding energy E_b of the graphdiyne-metal contact is defined as

$$E_b = (E_C + E_M - E_{C\text{-}M}) / N \qquad (3)$$

where E_C, E_M, and $E_{C/M}$ are the relaxed energy for pristine graphdiyne, the clean metal surface, and the combined system, respectively, and N is the number of interfacial carbon atoms in a supercell. The equilibrium interlayer distance $d_{C\text{-}M}$ is defined as the average distance from the innermost layer of metal to graphdiyne surface in the vertical direction of the interface. The minimum interatomic distance d_{min} is defined as the minimum atomic distance from the innermost layer atom of metal to graphdiyne surface atom. Adsorption of graphdiyne on Ni and Pd surfaces is strong with $E_b > 0.23$ eV and $d_{C\text{-}M} < 2.25$ Å. In contrast, adsorption of graphdiyne on Al, Ag, Cu, Au, Ir, and Pt surfaces is weak with $E_b < 0.12$ eV and $d_{C\text{-}M} > 2.8$ Å. Generally speaking, large $d_{C\text{-}M}$ corresponds to large d_{min}. One exception is the adsorption of graphdiyne on Pt, which has a larger $d_{C\text{-}M}$ of 2.88 Å, but d_{min} is smaller with a value 2.14 Å.

The electronic structures of graphdiyne adsorbed on Al, Ag, Cu, Au, and Ir surfaces are shown in Fig. 3 and those on Pt, Pd, and Ni surfaces are shown in Fig. 4. The band structure of graphdiyne is identifiable clearly on Al, Ag, Cu, and Au surfaces, but unidentifiable (or barely identifiable) on Ir, Pt, Pd, and Ni surfaces. We also calculated the electronic structures of the other two Au-graphdiyne interfaces, and they are hardly distinguishable with that in Fig. 3, as shown in Fig. S1. Combining the binding energy, the minimum interatomic distance, and the degree of band hybridization, we can identify adsorption of graphdiyne on Al, Ag, Cu, and Au surfaces as a weak physisorption with a small E_b, a large d_{min}, and a weak band hybridization, and on Ir and Pt surfaces as a weak chemisorption with a small E_b but a strong band hybridization, and on Ni and Pd surfaces as a strong chemisorption with a large E_b, a small d_{min}, and a strong band hybridization.

The band structures of graphdiyne absorbed on metals are related with the outmost

valence electron of metals. The band structure of graphdiyne adsorbed on Al is less intact than that on Ag, Cu, and Au, because the outmost $3p$ orbitals of Al is partially occupied, which slightly hybridizes with the states of graphdiyne above the Fermi level (E_F), whereas the outmost electrons of the other three metals are all partially filled s states. The band energy of graphdiyne is strongly hybridized with Ir, Pt, Pd, and Ni surfaces, because the outmost d occupied electrons of the four metals are strongly hybridize with the states near E_F of graphdiyne. The band gap of graphdiyne on Al, Cu, Au, and Ag surfaces are 0.31, 0.36, 0.39, and 0.47 eV, respectively, compared with a band gap of 0.46 eV in freestanding graphdiyne.

A vivid physical picture of the interaction at the metal-graphdiyne interface can be obtained by investigating the total electron density distributions for a slice that crosses both C atoms and metal atoms in real space. The total electron density distributions in real space of Ag-graphdiyne and Pd-graphdiyne interfaces are compared in Fig. 5. There is no electron accumulation between Ag and graphdiyne surface, suggesting absence of covalent bond between them. By contrast, electrons are accumulated between Pd and graphdiyne surfaces, indicating the formation of covalent bond between them. The difference confirms that the adsorption of graphdiyne on Ag is physisorption, with the band structure of graphdiyne intact, whereas that on Pd is chemisorption, with the band structure of graphdiyne distorted seriously.

Schottky barrier, tunneling barrier, and Fermi level pinning play important roles in a FET. The schematic diagram of a graphdiyne FET is shown in Fig. 6(a). Schottky barrier can appear on two different interfaces in a graphdiyne FET: One is between graphdiyne and the contacted metal surface in the vertical direction (labeled interface B, and the corresponding Schottky barrier height (SBH) is labeled Φ_V), and the other is between the contacted and the channel graphdiyne in the lateral direction (labeled interface D, and the corresponding Schottky barrier height is labeled Φ_L).[34] Other type of barrier can also occur at interface D if the band position between the contacted and the channel graphdiyne is different. Tunneling barrier can appear at interface B when electrons cross the gap (normally van der Waals gap) between metal and graphdiyne.

The absolute band position is an important metric to evaluate the SBH in

graphdiyne-metal interfaces. It is well known that DFT cannot estimate the band gap and thus the absolute band position of pristine semiconductor accurately, because it is a single-electron theory. Actually, the band gap of graphdiyne calculated by DFT and *GW* methods is 0.46 and 1.1 eV,[9] respectively. Many-electron effects must be taken into account to accurately predict the band structure of a semiconductor and they are even further enhanced with the reduced dimensionality [35,36,37,38,39]. A feasible method to determine the accurate band edge positions of a freestanding semiconductor is first-principles many-electron Green function approach within the *GW* approximation, where electron-electron correlation effects are treated properly, and the *GW* correction can give a band gap consistent with photoemission/inverse photoemission gap measurements. We propose that the Fermi level or the band gap center (BGC), namely, the average at the valence band maximum (VBM) and the conduction band minimum (CBM), is unchanged after *GW* correction, and the energy at CBM and VBM of graphdiyne after *GW* correction E_C^{GW} and E_V^{GW} can be obtained as

$$E_C^{GW} = E_F + \frac{1}{2}E_g^{GW} \tag{4}$$

$$E_C^{GW} = E_F - \frac{1}{2}E_g^{GW} \tag{5}$$

Where E_g^{GW} is the band gap of graphdiyne by *GW* approximation. E_F is the Fermi level of graphdiyne obtained by DFT method. Fig. 6(b) illustrates *GW* correction to the absolute band position. Such a correction scheme based on the unchanged BGC (termed *GW–BGC* scheme) has also been adopted to obtain the absolute band position by Jiang[40], Gong *etc.*[41] and Toroker *etc.*[42]. Actually, Yang *et al.*[43] found that the absolute band-edge energies for monolayer dichalcogenides given by the direct *GW* method and the *GW*-BGC scheme are quite similar. The calculated ionization potential (IP = $-E_V^{GW}$ = 5.45 eV) and electron affinity (χ = $-E_C^{GW}$ = 4.22 eV) of bulk MoS$_2$ by *GW–BGC* scheme,[40] compared with values of IP = 5.33 and χ = 4.45 eV from DFT–PBE functional,[40] are in good agreement with the experimental values (IP = 5.47 $\pm$0.15 eV and χ = 4.07 $\pm$0.35 eV).[44] Actually, it is reported in our early calculation that the band gap center of graphdiyne calculated by DFT and *GW* methods only differ by 0.05 eV .[9] Therefore, *GW–BGC* scheme is validated for graphdiyne.

As far as Φ_V is concerned, many-body effects are less significant[45,46], because the metal contact may greatly reduce electron-electron correlation especially if a large amount of charge transfer takes place and the DFT band edge positions and band gap are a good approximation. For example, the band gap at the Dirac point of heavily doped silicene only increases slightly from 0.34 to 0.38 eV upon the inclusion of the many-body effects[45,46]. Therefore, we do not make a *GW* correction in calculating Φ_V. But Φ_L depends on the band edge positions of the semiconducting channel, where electron-electron correlation is expected to remain or is affected insignificantly by dielectric under it[47]. It is found[47] that the quasiparticle band gap of monolayer $MoSe_2$ is only decreased from 2.26 eV (compared with a DFT value of 1.43 eV) in free-standing state to 2.13 ± 0.10 eV on semiconducting bilayer graphene (no charge transfer is expected between them), which in good agreement with the experimental value of 2.18 ± 0.04 eV for monolayer $MoSe_2$ on bilayer graphene[47].

Vertical SBH Φ_V is determined by the band structures of graphdiyne underneath metals and the Fermi level E_F of absorbed systems shown in Fig. 3 and Fig. 4. Because E_F of the absorbed systems is above the CBM of graphdiyne on Al, Ag, and Cu surfaces, there is no vertical metal-graphdiyne Schottky barrier for the three contacts at the two schemes. The Ohmic contact between graphdiyne and Al and Cu surfaces in the vertical direction has been measured by Li's group.[8] Nor does a vertical Schottky barrier exist for Ir, Pt, Ni, and Pd contacts at the two schemes because a strong band hybridization has taken place. By contrast, there is a quite small vertical Schottky barrier, which can be ignored, in terms of the difference between the E_F of absorbed systems and the CBM of graphdiyne underneath Au electrodes of $\Phi_v = 0.01$ eV.

Lateral SBH Φ_L is determined by the energy difference between the absorbed system E_F and the CBM (*n*-type) or the VBM (*p*-type) of channel graphdiyne. Graphdiyne forms an Ohmic contact with Al, Ag, and Cu in the lateral direction at DFT method since the absorbed system E_F is higher than CBM of channel graphdiyne at DFT method; After *GW*-BGC correction, the lateral Ohmic contact remains for Al contact but a rather small Schottky barrier appears for Ag and Cu contacts with $\Phi_L^{GW} = 0.02$ and 0.05 eV, respectively. Such a small SBH is probably blurred by thermionic emission at room temperature, and graphdiyne thus

forms a quasi-Ohmic contact with Ag and Cu in the lateral direction. The Fermi level of graphdiyne underneath metal is higher than CBM or lower than VBM of channel graphdiyne at DFT scheme, so Pd and Pt form lateral Ohmic contact with graphdiyne. After *GW*-BGC correction, a high lateral Schottky barrier is formed for Pd and Pt contacts, with $\varPhi_L^{GW}$ = 0.21 (*n*-type) and 0.30 (*p*-type) eV, respectively. There is a lateral *p*-type Schottky barrier for Ni and Ir-graphdiyne contacts at both DFT and *GW*-BGC schemes, with $\varPhi_L^{DFT}$ = 0.09 (Ni) and 0.14 (Ir) eV and $\varPhi_L^{GW}$ = 0.41 (Ni) and 0.46 (Ir) eV, and a *n*-type Schottky barrier for Au $\varPhi_L^{DFT}$ = 0.14 eV and $\varPhi_L^{GW}$ = 0.46 eV. In our calculations, the Schottky barrier directly calculated by DFT method is always much smaller than that by *GW*-BGC scheme because the band gap of graphdiyne calculated by DFT scheme of 0.46 eV are much smaller than that by *GW*-BGC scheme of 1.10 eV and the BGC of graphdiyne is assumed unchanged in the two schemes.

In our above calculations, we adapt the lattice constant of graphdiyne to that of Ni surface. Next, we explore the effects of the match way on the work function and the lateral SBH of Ni-graphdiyne interface by adapting the lattice constant of graphdiyne (1×1 unit cell) to that of Ni surface (4×4 unit cells). The buckling height of graphdiyne in this match way is smaller than that of the system with the lattice constant of Ni surface adjusted to that of graphdiyne, as shown in Fig. S2, because graphdiyne is stretched in this match way. The workfunction of the system with Ni surface adjusted to graphdiyne is only 0.12 eV larger than that of the system with graphdiyne adjusted to Ni surface, as a result the lateral SBH $\varPhi_L$ will be reduced by 0.12 eV without changing the doping type.

Fig. 2 shows the potential profiles at the vertical metal-graphdiyne interfaces. There is an obvious tunneling barrier (3.54 - 4.54 eV) at the metal-graphdiyne physisorption interfaces while there is a small (0.83 eV) or vanishing one at the metal-graphdiyne chemisorption interfaces. Similar results are found at the vertical metal-graphene interfaces.[48] Furthermore, we assume a square potential barrier to replace the real potential barrier, and the barrier height (ΔV) and width (w_B) of the square potential barrier are the barrier height and full width at half maximum (FWHM) of the real potential barrier shown in Fig. 2. The tunneling probabilities T_B is calculated using equation:[48]

$$T = \exp\left(-2 \times \frac{\sqrt{2m\Delta V}}{\hbar} \times w_B \right) \qquad (6)$$

where m is the massive of free electron and $\hbar$ is reduced the Plank's constant. The resulting tunneling possibilities at Au, Cu, Ag, Al, Ir, Pt, Ni, and Pd-graphdiyne interface are 4.79%, 6.36%, 6.83%, 7.15%, 8.11%, 21.55%, 71.35%, and 100%, respectively. The tunneling possibilities of chemisorption are much larger than those of physisorption.

In terms of the Schottky barrier and tunneling barrier, five types of metal-graphdiyne contacts are identified and shown in Fig. 6(c). In Type 1 contact, graphdiyne is in an Ohmic contact with Al electrodes with a large tunneling barrier at interface B, and in Type 2 contact, graphdiyne is in a quasi-Ohmic contact with Ag and Cu electrodes of a quite small Φ_L at interface D and a large tunneling barrier at interface B. Since the work function of Au is larger than those of Al, Ag, and Cu, electrons confront a small Schottky barrier Φ_V at interface B in addition to a large tunneling barrier and a large Schottky barrier Φ_L at interface D, leading to Type 3 contact. Pd, Ir, Ni, and Pt can form a covalent bond with graphdiyne and lead to the metallization of graphdiyne layer under them, thus eliminating the Schottky barrier Φ_V at interface B. In Ir, Ni, and Pt-graphdiyne contacts, electrons traverse a tunneling barrier at interface B and then confront a high Schottky barrier at interface D, forming Type 4 contact. In Pd-graphdiyne contact, there is only a lateral Schottky barrier Φ_L, resulting in a low-resistance Type 5 contact.

Fig. 7 shows the line-up of metal Fermi level with the electronic bands of graphdiyne after *GW* correction. There is no obvious Fermi level pinning in metal-graphdiyne contacts, while partial Fermi level pinning is calculated in MoS$_2$-metal contact[49,50] and graphdiyne-metal contact.[51] The Fermi levels of Al, Ag, Cu, Au, and Pd-graphdiyne absorbed systems are higher than that of the channel graphdiyne and form *n*-type contact, while the Fermi levels of Ir, Pt, and Ni-graphdiyne absorbed systems are lower than that of their channel graphdiyne and form *p*-type contact. Therefore, graphdiyne *p* - *n* junction can be fabricated by using Al, Ag, Cu, Au, or Pd to contact one end of graphdiyne and Ir, Pt, and Ni to contact the other end of it. Photoelectronic applications of graphdiyne can be developed.

Graphdiyne field effect transistor

To assess the electron transport performance of graphdiyne, we further simulate a graphdiyne FET in a top-gated two-probe model. We adopt Al as the electrodes in the following transport simulations because Al provides an Ohmic contact with graphdiyne in the vertical and lateral interface direction and Al electrode has actually be used. [8] The schematic model is presented in Fig. 6(a) and the distance between the Al lead and graphdiyne is 3.41 Å according to our DFT results. The dielectric region is made of SiO_2 with a thickness of 10 Å. To start with, we calculated the band structures of graphdiyne and the transmission spectrum of a 6 nm-channel-length graphdiyne FET using the DFT method with single-ζ (SZ) basis set to benchmark our semiempirical (SE) extended Hückel results (Fig. S3). The band structure and transmission spectrum calculated between the two methods are similar, especially the size and position of the band gap and transmission gap are highly consistent. Thus the SE approach is reliable and could be a good substitution of DFT in our transportation simulation. Then we focus on the transport properties of the graphdiyne FET with a larger channel length $L = 10$ nm. The transmission spectra of the device under $V_g = 0$ V is shown in Fig. 8(a). A transport gap of 0.47 eV appears below E_F and electrons are the majority charge carriers in this transistor, as expected from the calculated band alignment shown in Fig. 7. Therefore by applying a negative gate voltage to the channel, the conductance can be decreased, and an on-off switch is expected. The transmission coefficient of a FET $T(E)$, is proportional to the product of the projected density of states (PDOS) of electrodes and channel:[52]

$$T(E) \propto g_{ch}(E)g_L(E)g_R(E) \qquad (7)$$

where $g_{ch}(E)$ and $g_{L/R}(E)$ are the PDOS of the channel and the left/right lead, respectively. Therefore the transmission gap originates from the similar-sized PODS gap of the graphdiyne channel (Fig. 8(b)) and further originates from the band gap of infinite graphdiyne (0.46 eV).

As shown in Fig. 8(a), at $V_g = 0$ and -5 V an obvious transport gap of about 0.47 eV is located below E_F, leading to a large transmission coefficient at E_F ($T(E_F)$), while at $V_g = -7.1$ V, the gap is shifted to E_F, leading to a drastic decrease of $T(E_F)$. Fig. 8(c) shows the zero-bias transfer characteristics of the 10 nm-channel-length graphdiyne FET (σ vs. V_g), with an

apparent switching effect. The conductance decreases with increasing negative gate potential within $V_g = 0 \sim -0.71$ eV, typical of an *n*-type FET. The curve minimum, or the off state, is located at $V_g = -7.1$ V. If $V_g = -5$ V is chosen as the on-state, the on-off ratio can reach 10^4, which already satisfies the demand of FET used in complementary metal-oxide-semiconductor-like logic and is two orders of magnitude larger than the maximum on-off ratios obtained in the recently reported dual-gated bilayer[53] and ABC-stacked trilayer[54] graphene FET experiments. The steepest sub-threshold swing (SS) is 117 mV/dec. Although the SS is higher, it can be reduced by fabricating FET with a thin high-κ dielectric film (Al_2O_3 or HfO_2). The difference in the transport properties between the on- and off-state is also reflected from a difference of the transmission eigenchannel at $E = E_F$ and at the (0, 0) point of the *k*-space, as shown in Fig. 8(d). The transmission eigenvalue at $E = E_F$ and (0, 0) *k*-point under is 0.488 under $V_g = -5$ V, and the incoming wave function is scattered little and most of the incoming wave is able to reach to the other lead. By contrast, the transmission eigenvalue at this point nearly vanishes (1.836×10^{-5}) under $V_g = -7.1$ V, and the incoming wave function is nearly completely scattered and unable to reach to the other lead.

Fig. 8(e) presents the output characteristics of the 10 nm-channel-length graphdiyne FET acquired under $V_g = 0$ (the drain current density versus the bias voltage $J_{ds} - V_{bias}$). The linear behavior within 0.4 V bias indicates the formation of Ohmic contact between graphdiyne and Al leads, which is consistent with our DFT band calculation and previous experiments.[8] As this device is in two-contact configuration, we can estimate the upper limit for the contact

resistance by $R_c = \left. \dfrac{1}{2T_B} \dfrac{dV_{bias}}{dJ_{ds}} \right|_{V_{bias}=0} = 223$ Ω·μm. Although the small T_B (~7.15%) in

Al-graphdiyne contact which may induce a relatively larger contact resistance, the current density of the 10-nm-channel-length graphdiyne FET at $V_{bias} = 0.4$ V and $V_g = 0$ is as high as 1.3×10^4 mA/mm and already satisfies the requirement of 1480 mA/mm for the high performance FETs of 2020 from the 2013 edition of the International Technology Roadmap for Semiconductors (ITRS).[55] The large on-current in graphdiyne FETs is attributed to the high carrier mobility of graphdiyne[10] ($J \propto \mu$) and is beneficial to shorten the gate delay and

speed up the device operation. When V_{bias} is further increased, this 10 nm-channel-length graphdiyne FET exhibits a negative differential resistance (NDR) behavior, with a peak-to-valley ratio of 3 although no NDR is observed for long channel graphdiyne film.[8]

Computing technology requires a FET with channel length smaller than 10 nm in next decades, but bulk Si FET for some time will not perform reliably at sub-10 nm channel length, because short-channel effects are becoming more and more apparent, resulting in serious degradation of device performance and invalidation of Moore's law.[56] Graphdiyne is a possible substitute material for bulk Si at 10 nm channel length.[57] However, when the channel length decreases to 6 nm, the performance of the graphdiyne FET is greatly degraded: the on-off ratio is 10^2, and the steepest SS is 285 mV/dec (Fig. 8(c)). Therefore, the short-channel effect still remarkably affects the performance of sub-10 nm graphdiyne FETs. Besides, NDR behavior is also obtained in the 6 nm-channel-length graphdiyne FET, with a peak-to-valley ratio of 2. NDR can be applied in high frequency switches, oscillators, and memories, etc.

The transmission spectra of the 10 nm-channel-length graphdiyne FET as a function of V_{bias} are provided in Fig. 9(a) to give an insight into the observed NDR behavior. With the increasing V_{bias}, the transmission spectrum is shifted towards a higher energy. When $V_{bias} < 0.6$ V, the change of the transmission spectrum is insignificant. When $V_{bias} > 0.6$ V, the transmission coefficients are suppressed in both the valence and conductance bands, and another transport gap Δ_L occurs below the already existed gap Δ_R, with a roughly same size with Δ_R. Moreover, the gap Δ_R is elevated into the bias window. Simplified band diagram of the FET is provided in Fig. 9(b) - 9(d) to illustrate the change of the transmission spectra with the increasing V_{bias}. When $0 < V_{bias} < 0.6$ V the band profile of the channel is merely slightly affected (Fig. 9(c)) and so is the transmission spectrum. According to Eq. 2, the current increases with V_{bias}. As V_{bias} further increases, the electric potential difference between the two parts of the channel near the source and drain regions gets larger (Fig. 9(d)). As a result, the transport gaps induced by the band gaps in the two ends of the channel separate from each other (Δ_L and Δ_R), and the gap Δ_R is elevated into the bias window by the drain voltage. The tunneling across the middle part of the channel induces a much suppressed transmission hump between the two gaps Δ_L and Δ_R. The cause why the transmission coefficients above the gap

Δ_R (namely in the conduction band) is suppressed remains open. Because the gap Δ_R is moved into the bias window and the non-zero transmission probabilities in the bias window (above the gap Δ_R) are suppressed, the current starts to decrease, causing the NDR phenomenon.

Conclusions

We present the first systematic first-principles investigation on the interfacial properties of graphdiyne on a various metal substrates with inclusion of many-body effects based on a dual interface model. According to the adsorption strength and electronic structures, the contact of graphdiyne with Al, Ag, Cu, and Au surfaces is a physisorption, while with Ir and Pt surfaces is a weak chemisorption, and with Ni and Pd surfaces is a strong chemisorption. Graphdiyne is in an Ohmic or quasi-Ohmic contact with Al, Ag, and Cu surfaces, while a Schottky contact with Pd, Pt, Ni, Au, and Ir surfaces with lateral Schottky barrier heights of 0.21, 0.30, 0.41, 0.46, and 0.46 eV, respectively. Graphdiyne is *n*-type doped when contacted with Al, Ag, Cu, Au, and Pd electrodes, but *p*-type doped when contacted with Ir, Pt, and Ni electrodes. A quantum transport simulation is performed for a gated two-probe model made of graphdiyne contacted with Al electrodes, and a high current on-off ratio of 10^4 and a very large on-state current of 1.3×10^4 mA/mm are obtained. This fundamental study not only provides a deep insight into graphdiyne/metal contact but also reveals high performance of graphdiyne-based devices.

Acknowledgments

Supporting Information available

(1) Band structure of pure graphdiyne and graphdiyne adsorbed on Au surface of three kind configurations, (2) the comparison of optimized structure of the systems with Ni surface adjusted to graphdiyne and graphdiyne adjusted to Ni surface, (3) the comparison of the band structure of graphdiyne and the transmission spectra of a 6 nm-channel-length graphdiyne FET calculated by DFT and SE methods.

Notes and references

1.   H. W. Kroto, J. R. Heath, S. C. O'Brien, R. F. Curl and R. E. Smalley, *Nature*, 1985, **318**, 162-163.

2.   S. Iijima, *Nature*, 1991, **354**, 56-58.

3.   A. K. Geim and K. S. Novoselov, *Nat. Mater.*, 2007, **6**, 183-191.

4.   J. Zheng, Y. Wang, L. Wang, R. Quhe, Z. Ni, W. N. Mei, Z. Gao, D. Yu, J. Shi and J. Lu, *Sci. Rep.*, 2013, **3**, 2081. doi: 10.1038/srep02081.

5.   R. Quhe, J. Zheng, G. Luo, Q. Liu, R. Qin, J. Zhou, D. Yu, S. Nagase, W. N. Mei, Z. Gao and J. Lu, *NPG Asia Mat.*, 2012, **4**, e16; DOI:10.1038/am.2012.29.

6.   M. M. Haley, S. C. Brand and J. J. Pak, *Angew. Chem., Int. Ed.*, 1997, **36**, 863-866.

7.   Y. Li, L. Xu, H. Liu and Y. Li, *Chem. Soc. Rev.*, 2014, **43**, 2572-2586.

8.   G. Li, Y. Li, H. Liu, Y. Guo, Y. Li and D. Zhu, *Chem. Commun.*, 2010, **46**, 3256-8.

9.   G. Luo, X. Qian, H. Liu, R. Qin, J. Zhou, L. Li, Z. Gao, E. Wang, W.-N. Mei, J. Lu, Y. Li and S. Nagase, *Phys. Rev. B*, 2011, **84**.

10.   M. Long, L. Tang, D. Wang, Y. Li and Z. Shuai, *ACS Nano*, 2011, **5**, 2593-600.

11.   F. Schwierz, *Nat. Nanotechnol.*, 2010, **5**, 487-96.

12.   G. F. Luo, Q. Y. Zheng, W. N. Me, J. Lu and S. Nagase, *J. Phys. Chem. C*, 2013, **117**, 13072-13079.

13.   A. L. Ivanovskii, *Prog. Solid State Chem.*, 2013, **41**, 1-19.

14.   Q. Zheng, G. Luo, Q. Liu, R. Quhe, J. Zheng, K. Tang, Z. Gao, S. Nagase and J. Lu, *Nanoscale*, 2012, **4**, 3990-3996.

15.   H. Liu, J. Xu, Y. Li and Y. Li, *Acc. Chem. Res.*, 2010, **43**, 1496-1508.

16.   Y. Jiao, A. J. Du, M. Hankel, Z. H. Zhu, V. Rudolph and S. C. Smith, *Chem. Commun.*, 2011, **47**, 11843-11845.

17.   H. Du, Z. Deng, Z. Lü, Y. Yin, L. Yu, H. Wu, Z. Chen, Y. Zou, Y. Wang, H. Liu and Y. Li, *Synthetic Metals*, 2011, **161**, 2055-2057.

18.   N. L. Yang, Y. Y. Liu, H. Wen, Z. Y. Tang, H. J. Zhao, Y. L. Li and D. Wang, *ACS Nano*, 2013, **7**, 1504-1512.

19.   C. Sun and D. J. Searles, *J. Phys. Chem. C*, 2012, **116**, 26222-26226.

20.   H. Y. Zhang, Y. Y. Xia, H. X. Bu, X. P. Wang, M. Zhang, Y. H. Luo and M. W. Zhao, *J. Appl. Phys.*, 2013, **113**, 044309.

21.   G. Li, Y. Li, X. Qian, H. Liu, H. Lin, N. Chen and Y. Li, *J. Phys. Chem. C*, 2011, **115**, 2611-2615.

22.   N. Narita, S. Nagai, S. Suzuki and K. Nakao, *Phys. Rew. B*, 1998, 11009-11014.

23.   M. D. Segall, P. J. D. Lindan, M. J. Probert, C. J. Pickard, P. J. Hasnip, S. J. Clark and M. C. Payne, *J. Phys.: Condens. Matter*, 2002, **14**, 2717-2744.

24.   J. P. Perdew, K. Burke and M. Ernzerhof, *Phys. Rev. Lett.*, **1996**, **77**, 3865-3868.

25.   A. Tkatchenko and M. Scheffler, *Phys. Rev. Lett.*, 2009, **102**, 073005.

26.   G. Kresse and D. Joubert, *Phys. Rev. B*, 1999, **59**, 1758-1775.

27.   G. Kresse and J. Hafner, *Phys. Rev. B* 1993, **47**, 558-561.

28.   G. Kresse and J. Furthmüller, *Phys. Rev. B*, 1996, **54**, 11169-11186.

29.   H. J. a. P. Monkhorst, J.D, *Phys. Rev. B*, 1976, **13**, 5188-5192.

30.   J. Taylor, H. Guo and J. Wang, *Phys. Rev. B*, 2001, **63**, 245407.

31.   M. Brandbyge, J.-L. Mozos, P. Ordejón, J. Taylor and K. Stokbro, *Phys. Rev. B*, 2002, **65**, 165401.

32.   Atomistix toolkit version 11.2, quantum wise a/s: Copenhagen, denmark.

33.   M. Buttiker, Y. Imry, R. Landauer and S. Pinhas, *Phys. Rev. B*, 1985, **31**, 6207-6215.

34.   J. Kang, W. Liu and K. Banerjee, *Appl. Phys. Lett.*, 2014, **104**, 093106.

35.   R. S. Sundaram, M. Engel, A. Lombardo, R. Krupke, A. C. Ferrari, P. Avouris and M. Steiner, *Nano Lett.*, 2013, **13**, 1416-21.

36.   L. Wirtz, A. Marini and A. Rubio, *Phys. Rev. Lett.*, 2006, **96**, 126104.

37.   C.-H. Park, C. Spataru and S. Louie, *Phys. Rev. Lett.*, 2006, **96**, 126105.

38.   L. Yang, C.-H. Park, Y.-W. Son, M. Cohen and S. Louie, *Phys. Rev. Lett.*, 2007, **99**, 186801.

39.   L. Yang, J. Deslippe, C.-H. Park, M. Cohen and S. Louie, *Phys. Rev. Lett.*, 2009, **103**, 186802.

40.   H. Jiang, *J. Phys. Chem. C*, 2012, **116**, 7664-7671.

41.   C. Gong, H. Zhang, W. Wang, L. Colombo, R. M. Wallace and K. Cho, *Appl. Phys. Lett.*, 2013, **103**, 053513.

42.   M. C. Toroker, D. K. Kanan, N. Alidoust, L. Y. Isseroff, P. Liao and E. A. Carter, *Phys. Chem. Chem. Phys.*, 2011, **13**, 16644-16654.

43.   Y. Liang, S. Huang, R. Soklaski and L. Yang, *Appl. Phys. Lett.*, 2013, **103**, 042106.

44.   R. Schlaf, O. Lang, C. Pettenkofer and W. Jaegermann, *J. Appl. Phys.*, 1999, **85**, 2732-2753.

45.   R. Quhe, R. Fei, Q. Liu, J. Zheng, H. Li, C. Xu, Z. Ni, Y. Wang, D. Yu, Z. Gao and J. Lu, *Sci. Rep.*, 2012, **2**, 853. DOI: 10.1038/srep00853.

46.   J. Neaton, M. Hybertsen and S. Louie, *Phys. Rev. Lett.*, 2006, **97**, 216405.

47.   M. M. Ugeda, A. J. Bradley, S. F. Shi, F. H. da Jornada, Y. Zhang, D. Y. Qiu, W. Ruan, S. K. Mo, Z. Hussain, Z. X. Shen, F. Wang, S. G. Louie and M. F. Crommie, *Nat. Mater.*, 2014, **DOI: 10.1038/NMAT4061**.

48.   X. Ji, J. Zhang, Y. Wang, H. Qian and Z. Yu, *Phys. Chem. Chem. Phys.*, 2013, **15**, 17883-17886.

49.   C. Gong, L. Colombo, R. M. Wallace and K. Cho, *Nano Lett.*, 2014, **14**, 1714-1720.

50.   W. Chen, E. J. Santos, W. Zhu, E. Kaxiras and Z. Zhang, *Nano Lett.*, 2013, **13**, 509-514.

51.   K.-E. Byun, S. Park, H. Yang, H.-J. Chung, H. J. Song, J. Lee, D. H. Seo, J. Heo, D. Lee, H. J. Shin and Y. S. Woo, *IEEE NMDC*, 2012, 63-66.

52.   Z. Y. Ni, Q. H. Liu, K. C. Tang, J. X. Zheng, J. Zhou, R. Qin, Z. X. Gao, D. P. Yu and J. Lu, *Nano Lett.*, 2012, **12**, 113-118.

53.   F. Xia, D. B. Farmer, Y.-m. Lin and P. Avouris, *Nano Lett.*, 2010, **10**, 715-718.

54.   T. Khodkov, F. Withers, D. C. Hudson, M. F. Craciun and S. Russo, *Appl. Phys. Lett.*, 2012, **100**, 013114.

55.   The international technology roadmap for semiconductors. Http://www.Itrs.Net/links/2012itrs/home2012.Htm.

56.   S. E. Thompson and S. Parthasarathy, *Mater. Today*, 2006, **9**, 20-25.

57.   M. Ieong, B. Doris, J. Kedzierski, K. Rim and M. Yang, *Science*, 2004, **306**, 2057-2060.

58.   G. Giovannetti, P. A. Khomyakov, G. Brocks, V. M. Karpan, J. van den Brink and P. J.

Kelly, *Phys. Rev. Lett.*, 2008, **101**, 026803.

59. P. A. Khomyakov, G. Giovannetti, P. C. Rusu, G. Brocks, J. van den Brink and P. J. Kelly, *Phys. Rev. B*, 2009, **79**.

Table 1 Calculated interfacial properties of graphdiyne on metal substrates. a represents the cell parameters of the surface unit cells for various metals. Δa is the metal surface constant mismatch. The binding energy E_b is the energy of per carbon atom to remove graphdiyne from metal surface. The equilibrium distance d_{C-M} is the average distance between the contact metal-graphdiyne interfaces in the vertical direction of it. The minimum interatomic distance d_{min} is the minimum atomic distance from the innermost layer atom of metal to graphdiyne surface atom. W_M and W are the calculated work function for clean metals surface and adsorbed graphdiyne respectively. E_g is the band gap of graphdiyne, Φ_v is the Schottky barrier in vertical direction. Φ_L^{DFT} (Φ_L^{GW}) is the Schottky barrier in lateral direction by DFT (GW-BGC) methods. ΔV, w_B, and T_B are tunneling barrier height, tunneling barrier width, and tunneling possibility, respectively. The calculated work function of graphdiyne is W_G = 5.14 eV, which is much larger that a value of 4.5 eV for graphene.[58,59,4]

	Al	Ag	Cu	Au	Ir	Pt	Ni	Pd
a (Å)	9.92	10.01	8.85	9.99	10.22	9.61	9.97	9.53
Δa (%)	4.95	5.89	6.31	5.70	6.23	1.70	5.46	0.96
E_b (eV)	0.12	0.09	0.11	0.09	0.10	0.11	0.32	0.23
d_{C-M} (Å)	3.41	3.40	3.22	3.45	3.11	2.88	2.24	2.18
d_{min} (Å)	3.43	3.46	3.21	3.18	3.10	2.14	1.94	2.22
W_M (eV)	4.07	4.66	4.63	5.10	5.53	5.20	5.26	5.24
W (eV)	4.35	4.61	4.64	5.05	5.24	5.39	5.28	4.80
E_g (eV)	0.31	0.47	0.36	0.40	0.00	0.00	0.00	0.00
Φ_v (eV)	0.00	0.00	0.00	0.01	0.00	0.00	0.00	0.00
Φ_L^{DFT} (eV)	0.00	0.00	0.00	0.14	0.14	0.00	0.09	0.00
Φ_L^{GW} (eV)	0.00	0.02	0.05	0.46	0.46	0.30	0.41	0.21
ΔV （eV）	3.97	3.54	3.78	4.54	4.20	3.55	0.83	0.00
w_B (Å)	1.29	1.39	1.38	1.39	1.20	0.80	0.36	0.00
T_B (%)	7.15	6.83	6.36	4.79	8.11	21.55	71.35	100.00
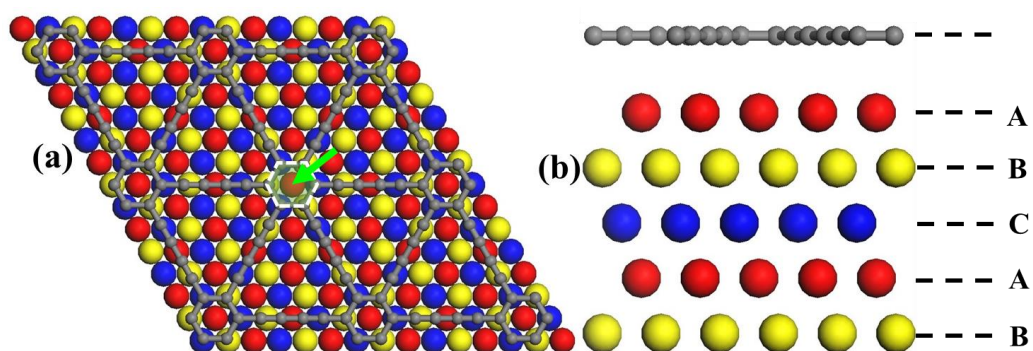
Fig. 1 (a) Top and (b) side views of the initial configuration of graphdiyne (gray balls) on metal surfaces (colored balls).
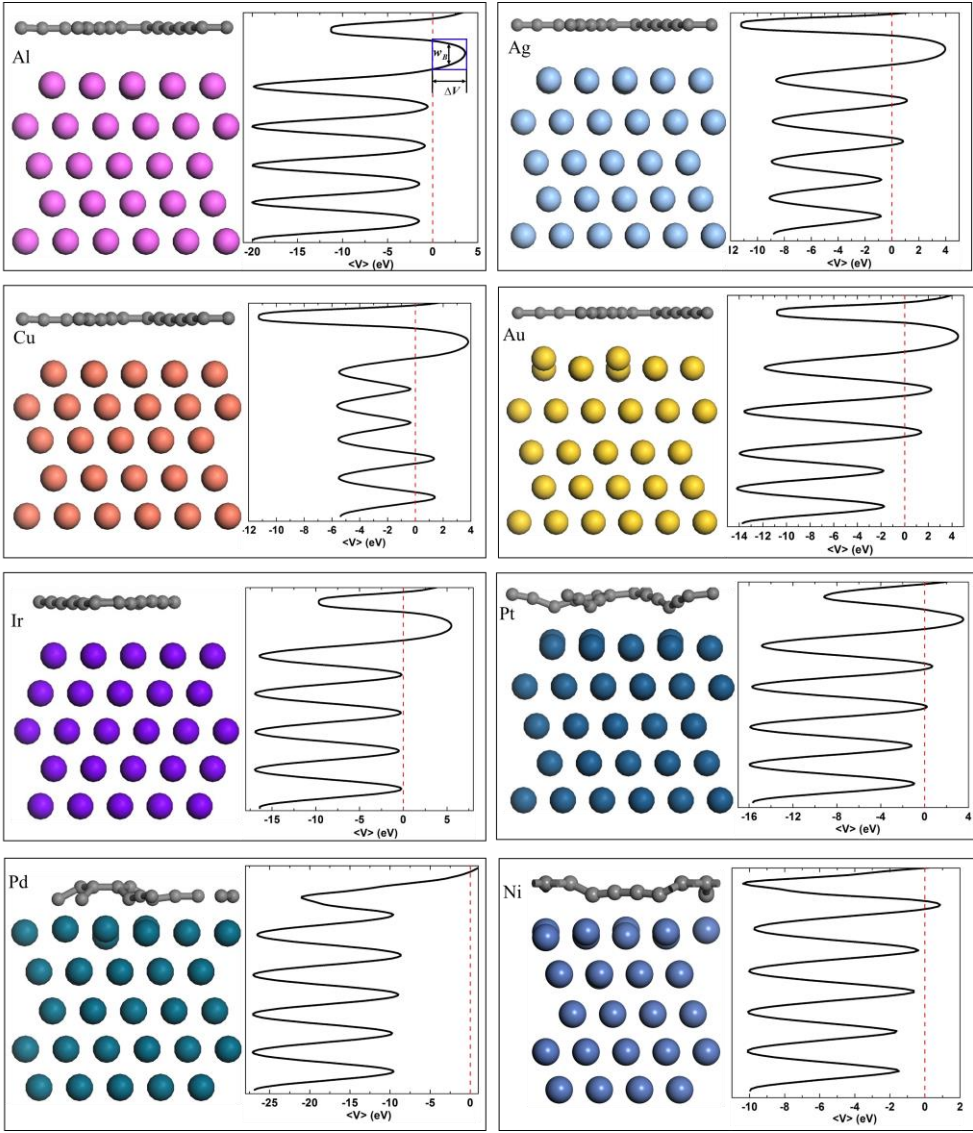
Fig. 2 Side view of the optimized structure and average electrostatic potential in planes normal to the interface of graphdiyne-Al, Ag, Au, Cu, Ir, Pt, Pd, and Ni systems, respectively. The Fermi level is set to zero.
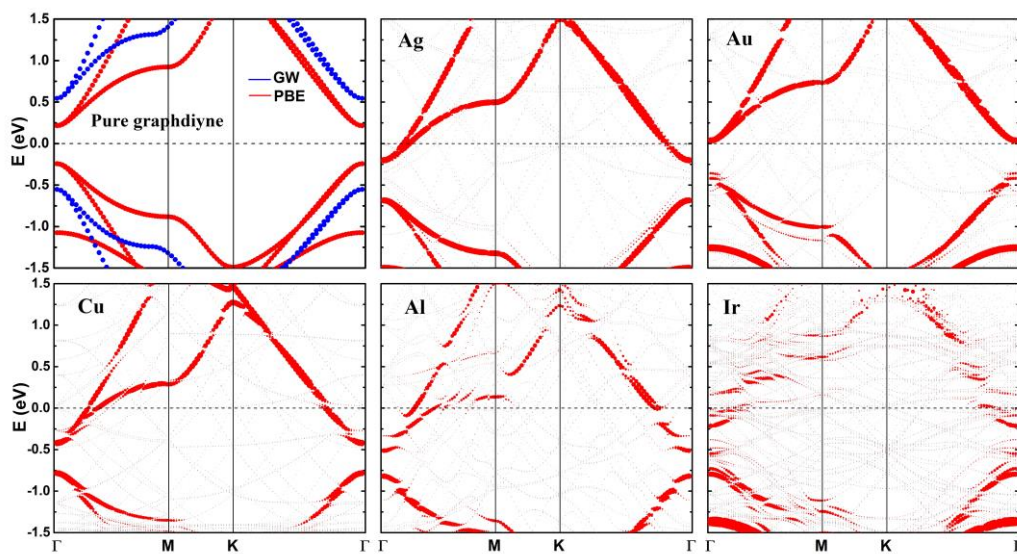
Fig. 3 Band structures of pristine graphdiyne (by DFT and *GW* methods) and graphdiyne adsorbed upon Al, Ag, Cu, Au, and Ir substrates by DFT method. The Fermi level is set at zero energy. Gray line: the bands of adsorbed systems; red line: the bands of graphdiyne. The line width is proportional to the weight.

22
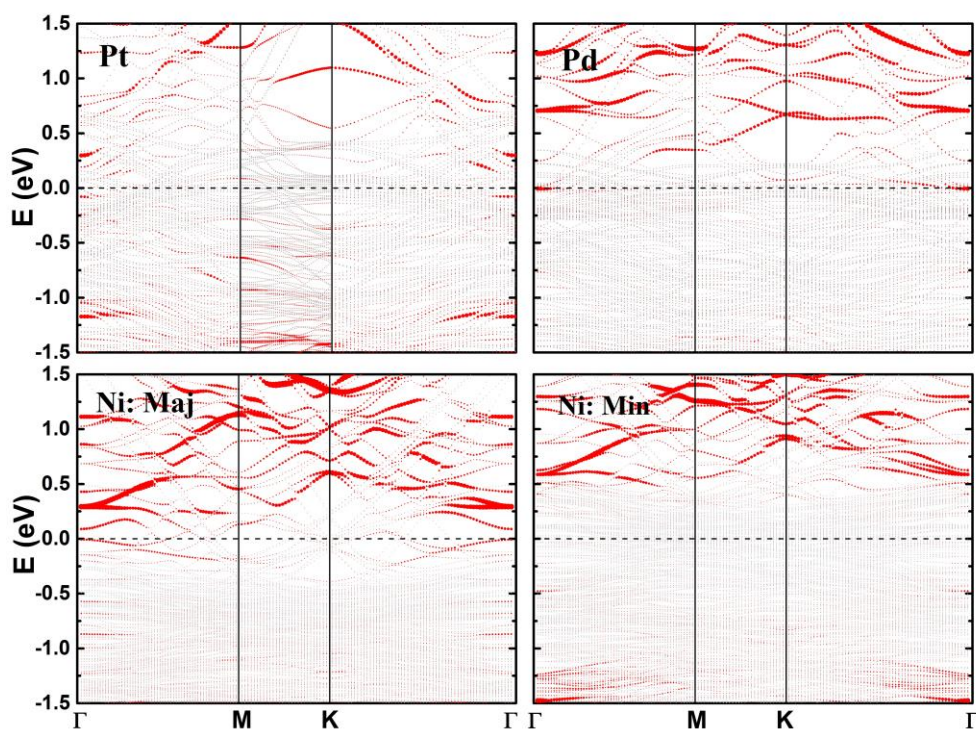
Fig. 4 Band structures of graphdiyne adsorbed upon Pt, Pd, and Ni substrates by DFT method. The Fermi level is set at zero energy. Gray line: the bands of adsorbed systems; red line: the bands of graphdiyne. The line width is proportional to the weight. The labels Maj/Min indicate the majority-spin and minority-spin bands of graphdiyne on Ni substrate.
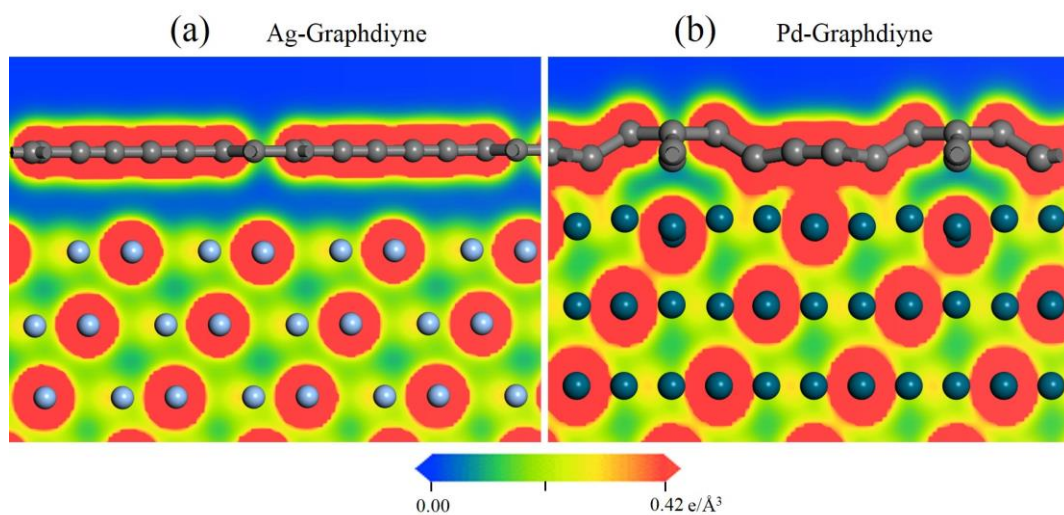
Fig. 5 Contour plots of total electron distribution of (a) Ag-graphdiyne and (b) Pd-graphdiyne interfaces. Grey, green, and blue balls are C, Ag, and Pd atoms, respectively.
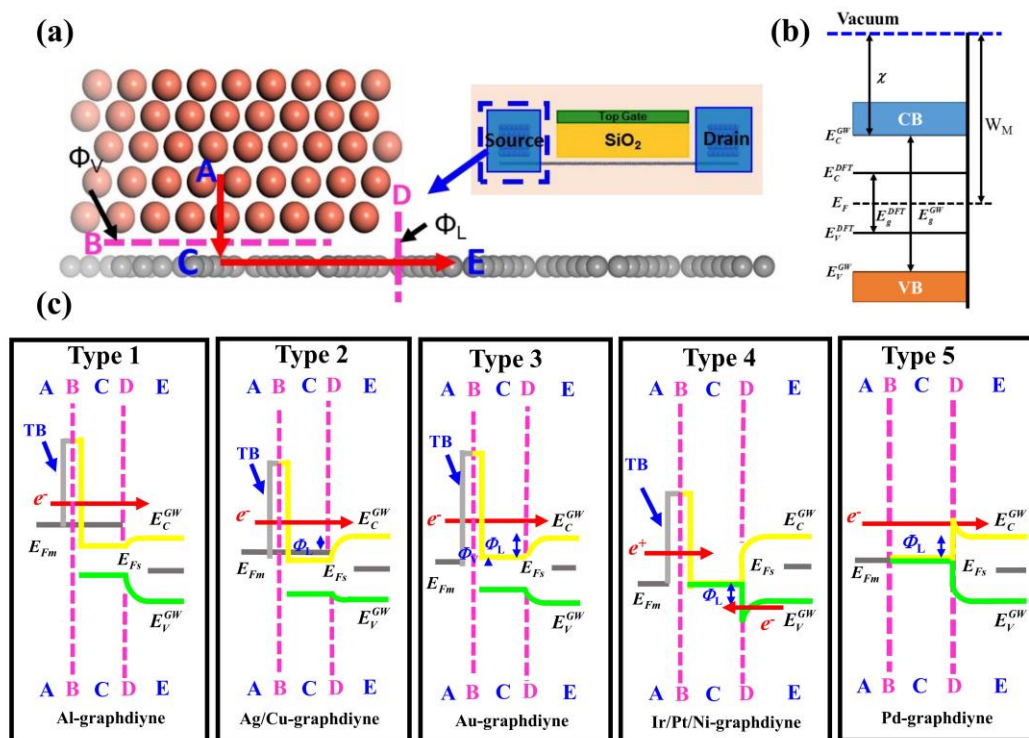
Fig. 6 (a) Right: Schematic diagram of a graphdiyne FET. Left: Schematic cross-sectional view of a typical metal contact to intrinsic graphdiyne channel. A, C, and E denotes three regions, while B and D are the two interfaces separating them. Red rows show the pathway (A⇨B⇨C⇨D⇨E) of electron or hole injection from contact metal (A) to the graphdiyne channel (E). Inset figure shows the source/drain contacts and the channel region in a typical top-gated FET. (b) Schematic illustration of the absolute band position with respect to the vacuum level by *GW* correction. (c) Five possible band diagrams of (a), depending on the type of metal. Examples are provided at the bottom of each diagram. E_{Fm} and E_{Fs} denote the Fermi level of absorbed system and channel graphdiyne, respectively.
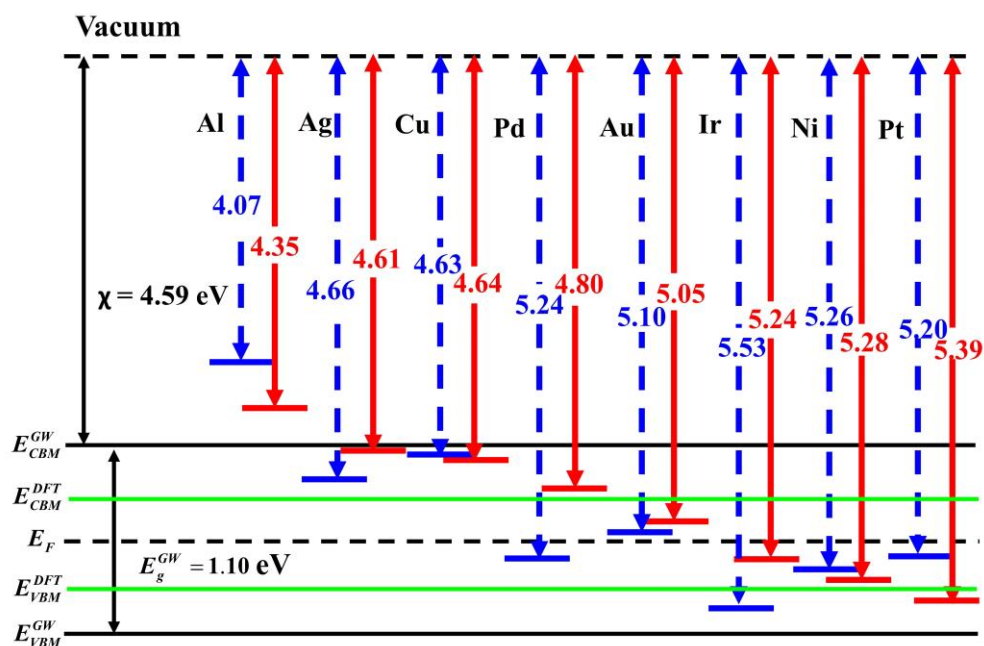
Fig. 7 Line-up of source work function with the DFT and *GW*-corrected electronic bands of channel graphdiyne. The blue dash line is the work function of pure metal, and the red solid line is the work function of contacted systems.
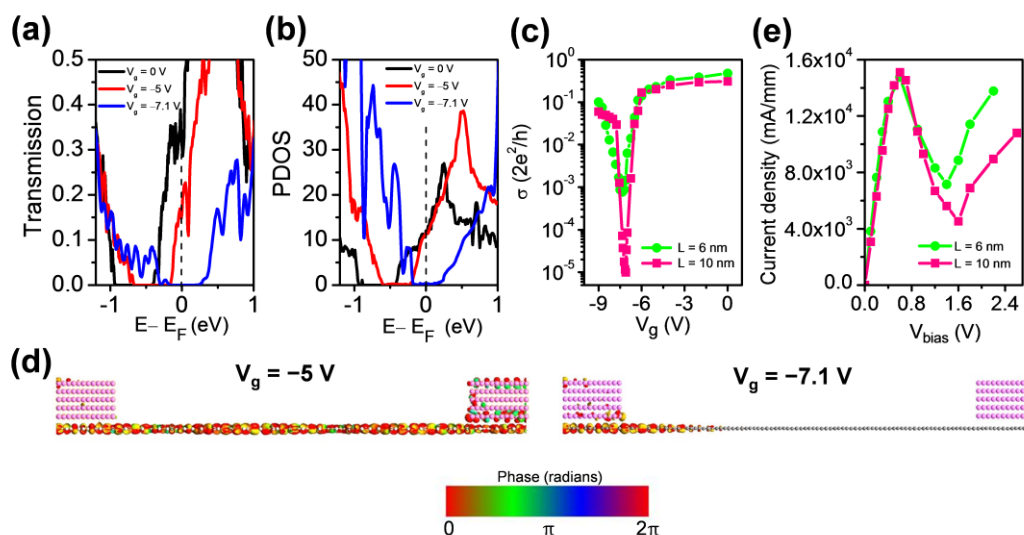
Fig. 8 Single-gated graphdiyne FET with Al electrodes: (a) Transmission spectra and (b) projected density of states of the channel under $V_g = 0$, -5, and -7.1 V in the graphdiyne FET with a channel length $L = 10$ nm. (c) Zero-bias transfer characteristics for $L = 6$ and 10 nm. (d) Transmission eigenstates at $E = E_F$ and at $k = (0, 0)$ for the on- ($V_g = -5$ V, left panel) and off-state ($V_g = -7$ V, right panel) with $L = 10$ nm. The isovalue is 0.2 a.u.. (e) Output characteristics of the 6 and 10 nm-channel-length graphdiyne FET under $V_g = 0$.
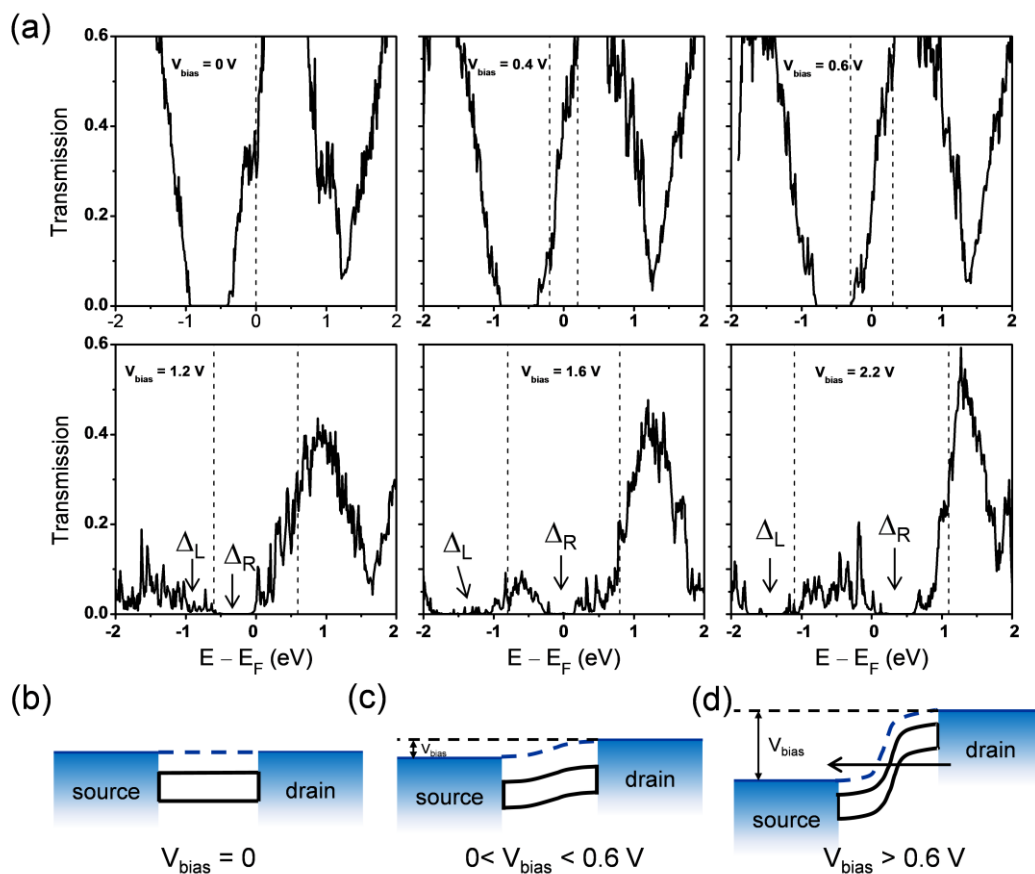
Fig. 9 (a) Transmission spectra and (b-d) band diagrams of the 10 nm-length-channel graphdiyne FET with Al electrodes under different V_{bias} (negative drain bias) at $V_g = 0$. The black dashed vertical line indicates the bias window. $\Delta_{L(R)}$ denotes the transport gap induced by the band gap in the left (right) part of the channel near the source (drain) region.